

High-Precision Indoor Localization via Dual-Modal AOA/TOA Fusion with Deep Learning and Particle Filters

Xiaoli YAO¹, Zhijiang XU², Fangfang QIANG³

¹Institute of Intelligent Transportation, Zhejiang Polytechnic University of Mechanical and Electrical Engineering, Binwen Rd. 528, 310053 Hangzhou, China

²School of Automation, Zhejiang Polytechnic University of Mechanical and Electrical Engineering, Binwen Rd. 528, 310053 Hangzhou, China

³School of Artificial Intelligence and Information Engineering, Zhejiang University of Science and Technology, Liuhe Rd. 318, 310023 Hangzhou, China

yaoxiaoli@zime.edu.cn, xuzhijiang@zime.edu.cn, qiangff_my@163.com

Submitted July 15, 2025 / Accepted September 15, 2025 / Online first October 24, 2025

Abstract. *As the era of IoT and artificial intelligence advances, the demand for high-precision indoor positioning systems continues to grow. Achieving accurate positioning in indoor environments remains challenging due to the presence of obstacles and signal interference, especially in Non-Line-of-Sight (NLOS) conditions. To address these challenges, this paper proposes a novel indoor positioning algorithm based on the fusion of Angle of Arrival (AOA) and Time of Arrival (TOA) data. A hybrid model combining Asymptotic Gradient Boosted Regression Trees (GBRT) and Elastic Net (EN) is used to reduce AOA measurement errors in NLOS environments, followed by the application of the Levenberg-Marquardt (LM) optimization algorithm to enhance localization accuracy. Experimental results show a significant reduction in positioning error, with an average error of 0.47 meters, representing a 41.25% improvement compared to the KF+WLS algorithm. Meanwhile, to improve TOA positioning, a deep learning-based TOA fingerprinting algorithm is proposed, this algorithm captures complex spatiotemporal features in TOA data, leading to a 25.00% and 15.22% reduction in root mean square error (RMSE) compared to the WKNN and WLS algorithms, respectively. Finally, a fusion strategy based on Particle Filtering (PF) is introduced to combine AOA and TOA data, achieving further RMSE reductions of 35.42% and 20.51%, compared to individual AOA and TOA methods.*

Keywords

Indoor localization, angle of arrival, time of arrival, machine learning, particle filter

1. Introduction

With the rapid progress of information technology and the widespread use of mobile internet, the application scope of positioning systems has expanded considerably in both indoor and outdoor settings. In fields such as intelligent

transportation, smart city management, and Location-Based Services (LBS), the requirements for positioning accuracy, reliability, and resistance to interference have become increasingly stringent and diverse.

For outdoor environments, satellite-based positioning technologies (including the Global Positioning System (GPS), the Global Navigation Satellite System (GLONASS) [1], and the BeiDou Navigation Satellite System (BDS) [2]) are widely used in commercial services, transportation, and public safety. Among these, GPS is the most mature and extensively deployed, fulfilling most outdoor localization needs.

However, a growing body of research indicates that human activities now occur more frequently indoors, where environmental complexity greatly weakens signal performance. Structural barriers such as walls, furniture, and building materials cause significant signal attenuation and multipath propagation, rendering satellite-based systems unreliable. As a result, GPS is often ineffective for indoor localization [3]. This limitation has created an urgent demand for alternative positioning technologies that can provide high accuracy, real-time operation, and robust performance under indoor conditions.

1.1 Related Works

Current indoor positioning techniques are mainly built on wireless signals, including Wireless Fidelity (Wi-Fi) [4], Bluetooth Low Energy (BLE) [5], Ultra-Wideband (UWB) [6] and LoRa (Long Range) technology [7]. Among these, LoRa stands out for its long communication range, low power consumption, strong resistance to interference, and low deployment costs, which make it particularly attractive for large-scale, low-power IoT applications. However, its low accuracy and limited data transmission rate make it unsuitable for high-precision localization tasks. Therefore, in practical applications, LoRa is well-suited for relatively simple localization scenarios that do not require high accuracy, such as warehouse management, smart building systems,

and asset tracking [8]. Each of these technologies has unique strengths and limitations, making them suitable for different use cases depending on accuracy requirements and deployment conditions. Indoor localization methods generally fall into two main categories: geometry-based methods and fingerprint-based methods. Geometry-based techniques are further divided into distance-based and angle-based approaches, utilizing parameters such as Time of Arrival (TOA), Time Difference of Arrival (TDOA), Time of Flight (TOF), Angle of Arrival (AOA) [9], and Angle of Departure (AOD) [10], [11]. These methods compute nonlinear relationships between measured parameters and the target's position, which are then solved using numerical optimization. In contrast, fingerprint-based methods collect wireless signal features at known reference points to create a database and use machine learning models to infer the location of unknown positions by matching real-time measurements.

Among geometry-based approaches, TOA and AOA are widely applied due to their relatively high precision and mature measurement techniques. Wan et al. proposed a novel antenna array design combined with signal processing techniques, significantly improving AOA positioning accuracy; however, the complex design increases both system cost and complexity [12]. Furfari et al. introduced an AOA-based indoor positioning system, optimizing multipath effects and enhancing system stability, but the AOA system still suffers from insufficient accuracy in NLOS environments [13]. Zhang et al. presented an improved TOA positioning algorithm that enhances positioning accuracy through multipath suppression and time synchronization optimization, though it remains limited in NLOS environments [14]. Zaidi et al. proposed a cooperative positioning scheme combining TOA and RSSI, improving accuracy and robustness by using variable anchor positions, but the method relies on precise synchronization and may suffer from multipath effects in NLOS environments, leading to decreased accuracy [15].

Despite these advancements, TOA- and AOA-based systems continue to face significant challenges in complex indoor environments. Dense obstacles and diverse interference sources often cause diffraction, scattering, and refraction, leading to severe NLOS propagation [16], which substantially degrades signal quality and prevents these systems from consistently meeting the requirements of high-precision indoor positioning.

1.2 Contributions

To address these challenges, this study proposes a hybrid indoor positioning framework based on the fusion of AOA and TOA. The main contributions are summarized as follows:

- **AOA Measurement Correction Based on GBRT-EN:** An enhanced algorithm is developed to correct large AOA errors commonly observed in NLOS environments. The method first applies a hybrid model that combines Gradient Boosting Regression Trees (GBRT) with Elastic Net (EN) to reduce NLOS-induced errors. Subsequently, the Levenberg-Marquardt

(LM) optimization algorithm is employed to refine the estimation and achieve accurate target localization.

- **TOA Fingerprinting Based on CNN-SA-LSTM:** A deep learning-based TOA fingerprinting method is proposed to mitigate positioning errors in complex indoor settings. The approach constructs a TOA fingerprint database and leverages a CNN-SA-LSTM network to establish the mapping between fingerprints and spatial positions. In this framework, CNN is responsible for spatial feature extraction, LSTM captures temporal dependencies, and a Self-Attention mechanism highlights key information in long sequences, thereby improving localization accuracy compared with traditional techniques.
- **AOA/TOA Fusion Using Particle Filtering:** To further enhance robustness, an AOA-TOA fusion algorithm based on Particle Filtering (PF) is designed. In this scheme, preliminary coordinate estimates are first obtained using the improved AOA correction and TOA fingerprinting methods. These results are then fused through PF, which performs nonlinear integration of the measurements to refine coordinate estimation and significantly improve overall positioning performance.

1.3 Organization

The remainder of this paper is structured as follows. Section 2 introduces the improvement of AOA accuracy using the GBRT-EN model together with the Levenberg–Marquardt optimization algorithm. Section 3 presents the refinement of TOA fingerprinting through deep neural networks to enhance positioning performance. Section 4 describes the fusion of AOA and TOA results using a particle filtering approach, which further improves localization accuracy and robustness. Section 5 outlines the experimental setup and reports the results, validating the effectiveness of the proposed framework.

2. AOA Localization Based on GBRT-EN and Levenberg–Marquardt Algorithms

Geometry-based indoor localization methods typically face two major challenges: (1) the nonlinear relationship between measurements and the target position, and (2) the adverse impact of complex indoor environments, which often leads to NLOS propagation and significantly increases localization errors. While effective algorithms exist for solving nonlinear equations under Line-of-Sight (LOS) conditions with high accuracy, their performance tends to degrade markedly in NLOS environments due to measurement distortion. To address this issue, a machine learning-based correction approach is introduced into the AOA localization process. Specifically, a hybrid algorithm combining Gradient Boosted Regression Trees (GBRT) and Elastic Net (EN) is proposed to mitigate AOA measurement errors caused by NLOS propagation [17–22].

The corrected AOA values are subsequently used in the Levenberg–Marquardt (LM) algorithm [23] for position estimation. This integrated framework not only reduces the inherent inaccuracies in traditional AOA-based measurements but also enhances the overall accuracy and robustness of the localization system.

2.1 AOA Localization Principle and NLOS Signal Propagation Model

With the rapid development of wireless communication technology, angle-based localization methods have gained increasing attention. The core idea of the AOA localization method is to use the AOA information, measured by a receiving antenna array, and combine it with the known positions of reference points to estimate the spatial location of the tag. The mathematical model is as follows in Fig. 1.

Taking a two-dimensional space as an example, as shown in Fig. 1, suppose the target is located in the region defined by two base stations $BS_1(x_1, y_1)$ and $BS_2(x_2, y_2)$. The angles of arrival at the two base stations are denoted as θ_1 and θ_2 , respectively. The tag's position (x, y) can be determined using the following equations:

$$\begin{cases} y - y_1 = (x - x_1) \tan \theta_1, \\ y - y_2 = (x - x_2) \tan \theta_2. \end{cases} \quad (1)$$

The tag's position can be obtained by solving the above system of equations.

The AOA localization method not only reduces the number of required positioning base stations but also avoids the accumulation of errors caused by varying signal propagation times. This method can provide very high localization accuracy in LOS conditions. However, in complex scenarios, when obstacles such as buildings, walls, or human bodies obstruct the direct path between the transmitter and receiver, signals are forced to propagate via NLOS mechanisms such as reflection, diffraction, or scattering [24]. As illustrated in Fig. 2, such propagation paths degrade signal quality at the receiver end. This issue is particularly severe for localization algorithms that assume direct LOS propagation, as the presence of NLOS conditions introduces considerable positioning errors. These errors can render traditional algorithms unsuitable for high-precision localization tasks, such as indoor navigation or emergency communication scenarios.

Assume the localization system contains N base stations. Let the coordinate of the i -th base station be $BS_i(x_i, y_i)$,

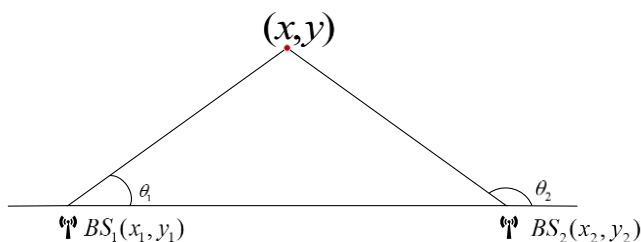


Fig. 1. AOA localization principle.

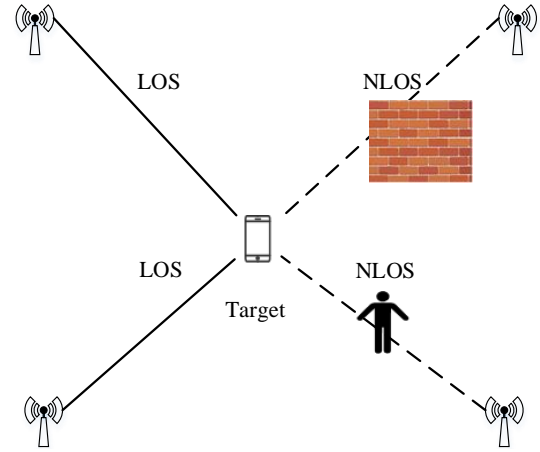


Fig. 2. Schematic diagram of NLOS signal propagation.

$i = 1, 2, 3, \dots, N$, the target location be $T(x, y)$, and the measured angle [30] between the i -th base station and the target be θ_i , then

$$\theta_i = \arctan \frac{y - y_i}{x - x_i} + n_i + e_i, \quad i = 1, 2, 3, \dots, N \quad (2)$$

where n_i represents measurement noise that follows a zero-mean Gaussian distribution, and e_i denotes a positive bias introduced by NLOS propagation.

In practical localization scenarios, AOA errors affected by NLOS conditions may follow various statistical distributions, including exponential, uniform, or Gaussian. The magnitude of these errors can range from a few degrees to several tens of degrees [25]. When raw AOA measurements are directly used for position estimation, significant localization errors can occur. Moreover, as the measurement distance increases, the likelihood of encountering obstacles along the propagation path grows, leading to more severe NLOS effects and larger angular deviations. According to (2), the AOA from the target to the i -th base station can be modeled as:

$$\theta_i = \theta_i^0 + \text{los}_i + \text{nlos}_i, \quad i = 1, 2, 3, \dots, N \quad (3)$$

where θ_i^0 denotes the true AOA, los_i represents the measurement noise under LOS conditions, which follows a zero-mean Gaussian distribution, and nlos_i accounts for the AOA error caused by NLOS propagation.

Under different radio propagation conditions, NLOS errors may follow different statistical distributions. Taking the exponential distribution as an example, its probability density function [30] is given in (4):

$$P = \begin{cases} \frac{1}{\theta_{i,\text{rms}}} \exp\left(-\frac{\text{nlos}_i}{\theta_{i,\text{rms}}}\right), & \text{nlos}_i > 0 \\ 0, & \text{nlos}_i \leq 0 \end{cases} \quad (4)$$

where $\theta_{i,\text{rms}}$ denotes the root mean square angular error under different channel conditions, which can be expressed as [31]:

$$\theta_{i,\text{rms}} = \partial_1 d_i^e \xi \quad (5)$$

where ∂_1 is the median RMSAE, d_i is the distance between

the tag and the i -th base station, ε is a constant ranging from 0.5 to 1, and ζ is a random variable following a normal distribution with zero mean and variance σ_ζ^2 .

In summary, directly using AOA measurements for position estimation under NLOS conditions can easily introduce substantial localization errors, leading to a significant decline in accuracy. Therefore, to enhance both the accuracy and reliability of localization, it is essential to develop effective algorithms that can mitigate AOA errors caused by NLOS propagation.

2.2 AOA Correction Algorithm Based on GBRT-EN

This paper proposes a machine learning-based correction method, in which a fusion algorithm is employed to mitigate the significant AOA errors caused by NLOS propagation. In NLOS scenarios, AOA errors generally exhibit nonlinear characteristics that traditional algorithms find challenging to accurately model and correct. In contrast, machine learning models inherently possess stronger nonlinear approximation capabilities by learning complex propagation patterns from historical datasets. Among these models, GBRT model is particularly advantageous due to its ensemble learning architecture, which progressively reduces prediction errors, provides effective feature selection, and demonstrates robust noise immunity.

Leveraging these strengths, we propose a GBRT-EN-based algorithm to specifically reduce the NLOS-induced errors in AOA measurements. The proposed method initially employs the GBRT model for preliminary correction of AOA measurements, subsequently utilizing an EN model for further error compensation, thereby effectively smoothing abrupt angular variations. The application of the GBRT method for correcting AOA measurements involves two distinct phases: offline training and online estimation.

In the offline training phase, we construct a training dataset denoted as $\{(x_1, y_1), (x_2, y_2), \dots, (x_M, y_M)\}$ to optimize the parameters of the GBRT algorithm. In this dataset, each training sample $\{x_i, y_i\}_{i=1}^M$ is defined as follows:

The input vector $\mathbf{x}_i = [\theta_1^i, \theta_2^i, \dots, \theta_N^i]$ consists of the measured AOA values for the i -th sample, where N represents the number of base stations.

The target vector $\mathbf{y}_i = [\tilde{\theta}_1^i, \tilde{\theta}_2^i, \dots, \tilde{\theta}_N^i]$ comprises the corrected AOA values (i.e., AOA after NLOS error removal). These corrected values are obtained through geometric relationships between known sample positions and corresponding base station coordinates.

Due to the complexity of indoor environments, angle fluctuations may occur when correcting AOA measurements using the GBRT algorithm during the online estimation stage. Particularly in dynamic positioning scenarios, such fluctuations can compromise measurement stability and subsequently degrade localization accuracy. To address this issue, an EN model is introduced for error compensation. The

EN model, an extension of linear regression, incorporates both L1 and L2 regularization terms into its objective function to penalize regression coefficients, thereby optimizing the regression model. Specifically, L1 regularization facilitates feature selection by identifying and retaining significant variables, whereas L2 regularization mitigates overfitting by controlling the magnitude of coefficients. By combining these regularization techniques, the Elastic Net effectively enhances the accuracy of error compensation, balancing model complexity and predictive performance. Consequently, this combined approach significantly suppresses angle fluctuations, enhancing the smoothness and stability of the corrected AOA measurements.

During the estimation phase, a small amount of data is collected to construct a new error dataset $S = \{\tilde{\theta}_i, \Delta\theta_i\}$, where $\tilde{\theta}_i$ represents the estimated AOA measurement of the i -th sample obtained from the GBRT algorithm, and $\Delta\theta_i$ denotes the error between the estimated and true AOA value. Based on the newly formed dataset S , an EN model is used to predict the error term $\Delta\theta_i$, yielding the corresponding predicted value $\Delta\hat{\theta}_i$. The EN model is trained to minimize the following loss function:

$$J(\mathbf{w}) = \underset{\mathbf{w}}{\operatorname{argmin}} \left\{ \sum_{i=1}^S (\Delta\theta_i - P_w(\tilde{\theta}_i))^2 + \rho \sum_{j=1}^J [\alpha w_j^2 + (1-\alpha)|w_j|] \right\} \quad (6)$$

where $P_w(\tilde{\theta}_i)$ is a polynomial predictor for the error term $\tilde{\theta}_i$, modeled as a function of $\tilde{\theta}_i$. It is expressed as:

$$P_w(\tilde{\theta}_i) = w_0 + w_1\tilde{\theta}_i + w_2\tilde{\theta}_i^2 + \dots + w_{j-1}\tilde{\theta}_i^{j-1} + w_j\tilde{\theta}_i^j \quad (7)$$

where $\mathbf{w} = [w_1, w_2, \dots, w_j]$ represents the coefficient vector of the polynomial; ρ is a regularization parameter that controls the strength of the penalty; α in $(0, 1)$ determines the relative weight between L1 and L2 regularization components.

By training the EN model on the dataset, the optimal coefficient vector \mathbf{w} is obtained, which is then used to predict the value $\Delta\hat{\theta}_i$. Adding this predicted error to the GBRT output yields the final corrected AOA estimate $\hat{\theta}_i$, as expressed in (8):

$$\hat{\theta}_i = \tilde{\theta}_i + \Delta\hat{\theta}_i. \quad (8)$$

In the estimation phase, the output of the GBRT algorithm is an $L \times M$ -dimensional matrix \mathbf{G}_{out} :

$$\mathbf{G}_{\text{out}} = \begin{bmatrix} \tilde{\theta}_1^1 & \tilde{\theta}_2^1 & \dots & \tilde{\theta}_N^1 \\ \tilde{\theta}_1^2 & \tilde{\theta}_2^2 & \dots & \tilde{\theta}_N^2 \\ \vdots & \vdots & \vdots & \vdots \\ \tilde{\theta}_1^L & \tilde{\theta}_2^L & \dots & \tilde{\theta}_N^L \end{bmatrix} \quad (9)$$

where L denotes the number of data points generated during the localization process. By converting these data points into row vectors and concatenating them, a one-dimensional matrix $[\tilde{\theta}_1^1, \tilde{\theta}_2^1, \dots, \tilde{\theta}_{N-1}^L, \tilde{\theta}_N^L]^T$ is formed, which constitutes the constructed error dataset.

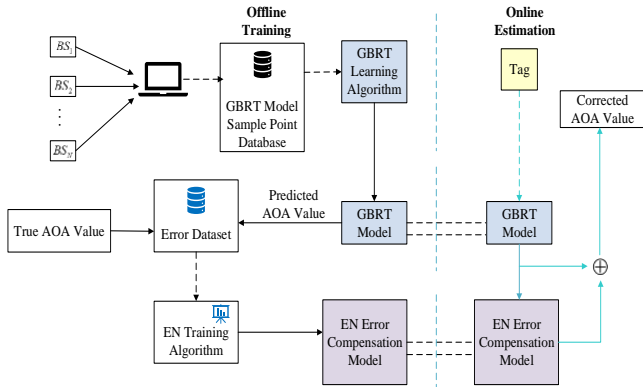


Fig. 3. Schematic diagram of the GBRT-EN-based AOA correction algorithm.

Based on the aforementioned methodology, Figure 3 illustrates the overall framework of the GBRT-EN-based AOA correction algorithm. The diagram is divided into two key phases: offline training and online estimation.

- Offline Training Phase:

In this phase, the system collects sample data, which is then stored in the GBRT model sample point database. The GBRT learning algorithm is applied to this data to predict the AOA values. Additionally, an error dataset is generated by comparing the predicted AOA values with the true AOA values. This dataset is then used to train the EN error compensation model.

- Online Estimation Phase:

During the online estimation phase, the trained GBRT model is used to estimate the AOA value based on the input from the tag location. The AOA value is then corrected using the EN error compensation model to obtain the final corrected AOA value.

This framework combines the strengths of GBRT for regression and EN for error compensation, aiming to enhance AOA-based positioning accuracy, particularly in complex indoor environments.

2.3 AOA Localization Based on the LM Algorithm

- Principle of the LM Algorithm

The LM algorithm is an optimization technique primarily used to solve nonlinear least squares problems [26]. It adopts a trust-region search strategy in which, during each iteration, a trust region is defined with a radius determined by the upper bound of step size. Taking the current iteration point as the center, a spherical trust region is constructed. The algorithm then seeks to solve the subproblem within this region, known as the trust-region subproblem, to find the point that minimizes the model function within the defined bounds.

Let the current iteration point be denoted by x_i , and let $r(x)$ represent the residual at point x_i . The first-order derivative is denoted by J_i and the second-order derivative is denoted by H_i . The trust-region subproblem [30] can be formulated as follows:

$$\min_d m_i(\mathbf{d}) = \mathbf{r}_i + \mathbf{J}_i^T \mathbf{d} + \frac{1}{2} \mathbf{d}^T \mathbf{H}_i \mathbf{d} \quad \text{s.t. } \|\mathbf{d}\| \leq \mu \quad (10)$$

where d is the trial step direction, μ is the trust-region radius.

Equation (13) describes the process of finding a trial direction d_i near the current point x_i , such that the objective function achieves sufficient descent along that direction while still satisfying the trust-region constraint.

Typically, during the i -th iteration, the ratio ρ_i between the actual reduction in the objective function and the predicted reduction from the model function is used to determine whether the trial step d_i should be accepted, and how the trust-region radius μ should be updated accordingly.

$$\rho_i = \frac{r(\mathbf{x}_i) - r(\mathbf{x}_i + \mathbf{d}_i)}{m_i(0) - m_i(\mathbf{d}_i)}. \quad (11)$$

If the computed ratio ρ_i exceeds a predefined threshold, it indicates that the model function sufficiently approximates the actual objective function. In this case, the trial step d_i is accepted, and the trust-region radius μ is increased to allow for a broader search space in the next iteration. Conversely, if ρ_i falls below the threshold, the model function is deemed to poorly represent the true objective, and the trial step d_i is rejected. The algorithm retains the current iteration point x_i and reduces the trust-region radius μ to conduct a more refined local search.

This iterative process is repeated until the change in position Δx satisfies a predetermined precision threshold μ , at which point the algorithm terminates and outputs the estimated location of the target tag.

- AOA Localization Algorithm Based on the LM Method

The overall workflow of the proposed AOA localization algorithm, which integrates GBRT-EN correction with LM optimization, is illustrated in Fig. 4. First, the raw AOA measurements are preliminarily corrected using the GBRT model. Then, the corrected measurements are further refined through error compensation using the EN model. Finally, the target position is estimated using the LM algorithm, thus completing the localization process.

In the LM algorithm, the trust-region radius μ is introduced to constrain the step length. This yields:

$$\Delta \mathbf{s} = -(\mathbf{H} + \mu \mathbf{I})^{-1} \mathbf{J}^T \mathbf{r}(\mathbf{s}). \quad (12)$$

Assume that in the i -th iteration, the estimated position of the target tag is $\mathbf{s}_i = [x_i, y_i]^T$, and the trust-region radius is

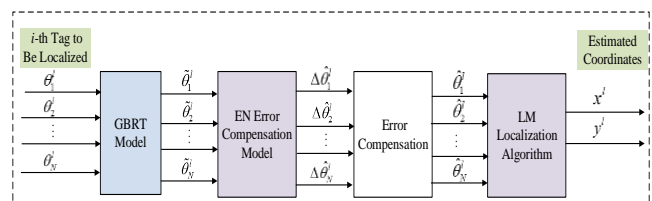


Fig. 4. Workflow of the AOA localization algorithm based on GBRT-EN and LM.

μ_i . At the current iteration point \mathbf{s}_i , the model function $D_i(d)$ is constructed as:

$$\min_{\mathbf{d}} D_i(\mathbf{d}) = f_i + \mathbf{J}_i^T \mathbf{d} + \frac{1}{2} \mathbf{d}^T \mathbf{H}_i \mathbf{d}, \quad \text{s.t. } \|\mathbf{d}\| \leq \mu, \mu > 0. \quad (13)$$

$$\text{Let: } \rho_i = \frac{f(\mathbf{s}_i) - f(\mathbf{s}_i + \mathbf{d}_i)}{D_i(0) - D_i(\mathbf{d}_i)}.$$

That is:

$$\rho_i = \frac{\arctan\left(\frac{y + \Delta y - y_i}{x + \Delta x - x_i}\right) - \arctan\left(\frac{y - y_i}{x - x_i}\right)}{\mathbf{J}_i^T \mathbf{d} + \frac{1}{2} \mathbf{d}^T \mathbf{H}_i \mathbf{d}} \quad (14)$$

where ρ_i represents the ratio between the actual reduction in the objective function and the predicted reduction given by the model function in the i -th iteration. This ratio reflects how well the quadratic model approximates the true behavior of the objective function.

The optimal solution to the trust-region subproblem is defined as $\mathbf{d}_i = [\Delta x_i, \Delta y_i]^T$, referred to as the trial step. The value of ρ_i is used to determine whether to accept the trial step d_i , as well as how to update the trust-region radius μ . Theoretically, the closer ρ_i is to 1, the better the approximation performance of the model function; conversely, when ρ_i approaches 0, it indicates poor approximation quality. In practical applications, however, considering both empirical experience and the balance between algorithmic convergence and efficiency, threshold values of $\rho_i = 0.75$ and $\rho_i = 0.25$ are typically adopted. When $\rho_i > 0.75$, it implies that the actual reduction closely matches the predicted reduction, indicating that the model function accurately approximates the real objective. In this case, the trial step d_i is accepted, and the trust-region radius μ is doubled to allow a broader search space in the next iteration. When $\rho_i < 0.25$, it suggests that the actual reduction is far less than the predicted one, reflecting a poor model approximation. As a result, the trial step d_i is rejected, the current iteration point \mathbf{s}_i is retained, and the trust-region radius μ is halved to enable finer local search.

Accordingly, if $\rho_i > 0.75$, then $\mathbf{s}_{i+1} = \mathbf{s}_i + d_i$ and $\mu = 2\mu_i$; if $\rho_i < 0.25$, then $\mathbf{s}_{i+1} = \mathbf{s}_i$ and $\mu = 0.5\mu_i$. This iterative process continues until the step norm $\|\Delta \mathbf{s}\| = \|\Delta x, \Delta y\|^T$ satisfies the precision threshold $\varepsilon = 10^{-3}$, at which point the optimization terminates and the estimated tag position is output.

3. TOA Fingerprint-Based Localization Algorithm Using Deep Learning

The core principle of fingerprint-based localization algorithms lies in establishing an accurate mapping between signal fingerprints and spatial coordinates. Traditional matching-based approaches are highly sensitive to the density of fingerprint data collection, often resulting in significant positioning errors. On the other hand, model-based

methods are vulnerable to the inherent variability in fingerprint data. To address these limitations, a TOA fingerprint-based indoor localization algorithm is proposed based on deep learning techniques [27]. This approach leverages the ability of deep learning to automatically identify complex nonlinear signal patterns and learn the deep-level relationships between signal fingerprints and coordinates.

The central idea involves preprocessing TOA fingerprint data to construct a fingerprint database, followed by designing a deep learning-based localization model that integrates Convolutional Neural Networks (CNN), Long Short-Term Memory (LSTM) [28], and a self-attention mechanism [29]. Once trained, the model can directly estimate the coordinates of unknown points by inputting their corresponding fingerprint data.

3.1 TOA Fingerprint-Based Indoor Localization Model

The TOA localization method determines the distance by measuring the propagation time of the signal from the transmitter to the receiver and calculating the distance using the signal propagation speed. The tag's position is then determined through multilateration. The mathematical model is given by (15):

$$d = c \cdot (t_R - t_T). \quad (15)$$

Here, d is the propagation distance, c is the signal propagation speed, t_R is the signal reception time, and t_T is the signal transmission time.

As shown in Fig. 5, in a two-dimensional plane, the TOA-based positioning system typically uses trilateration to calculate the tag's position. The positioning area contains three base stations, denoted as $BS_i = (x_i, y_i)$, $i = 1, 2, 3$, with the tag's position being (x, y) . Assume the transmission time of the signal from the tag is t_0 , and the time for the signal to reach the i -th base station is denoted as t_i . The distance from the tag to the i -th base station is then calculated as:

$$d_i = c \cdot (t_i - t_0), i = 1, 2, 3. \quad (16)$$

The nonlinear system of equations for the tag's position (x, y) is established based on the above ranging values, as in (17):

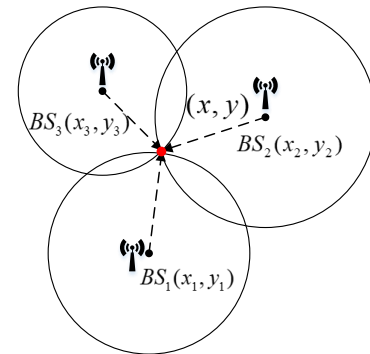


Fig. 5. TOA trilateration localization principle.

$$\begin{cases} d_1^2 = (x_1 - x)^2 + (y_1 - y)^2 \\ d_2^2 = (x_2 - x)^2 + (y_2 - y)^2 \\ d_3^2 = (x_3 - x)^2 + (y_3 - y)^2 \end{cases} \quad (17)$$

By solving the above equations, the position coordinates of the tag can be estimated.

In practical positioning, since the signal propagation speed is constant, the calculation of communication distance primarily relies on the TOA values of the signals. This places high demands on the time synchronization accuracy between the tag and the base stations. The fingerprint-based indoor localization model establishes a mapping between environmental features and physical coordinates to estimate target positions. In this study, TOA data is selected as the primary fingerprint feature due to its location-dependent variability. A TOA fingerprint-based localization model is constructed using this information and combined with a suitable learning algorithm to perform position estimation.

The localization process is divided into two phases: an offline phase and an online phase. In the offline phase, a TOA fingerprint database is constructed. Based on the size of the localization area, reference points are evenly deployed across the environment with an inter-point spacing of 0.50 meters. This spacing is chosen to balance the trade-off between positioning accuracy and data collection cost. The arrangement and numbering of the reference points are illustrated in Fig. 6.

Before constructing the TOA fingerprint database, the reference point data must undergo denoising and normalization preprocessing to improve data quality. This preprocessing enhances the distinctiveness of fingerprint features while preserving the spatial diversity of each reference point's characteristics, ensuring that the constructed database can accurately reflect position-dependent properties.

Subsequently, each reference point's TOA data is matched with its corresponding ground truth coordinates, and the paired data is stored in a matrix form as the fingerprint database, which supports model training for localization.

Assume that there are N TOA base stations and M reference points are deployed in the localization area. Let $TOA_{i,j}$ denote the TOA measurement collected at the i -th reference point from the j -th base station, and (x_i, y_i) represent the actual physical coordinates of the i -th reference point.

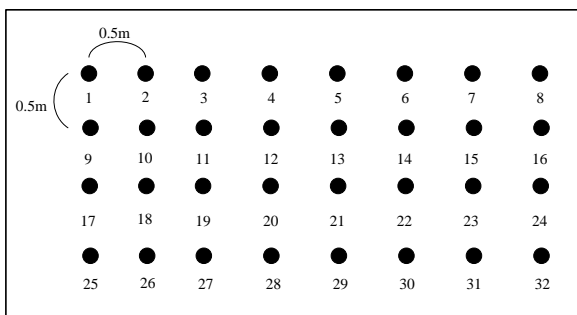


Fig. 6. Schematic diagram of reference point selection.

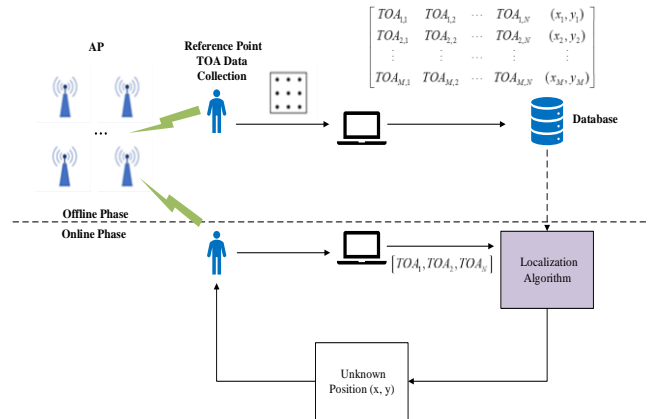


Fig. 7. Schematic diagram of the TOA fingerprint-based localization principle.

Then, the constructed fingerprint dataset ϕ can be expressed as in (18):

$$\phi = \begin{bmatrix} TOA_{1,1} & TOA_{1,2} & \dots & TOA_{1,N} & (x_1, y_1) \\ TOA_{2,1} & TOA_{2,2} & \dots & TOA_{2,N} & (x_2, y_2) \\ \vdots & \vdots & \dots & \vdots & \vdots \\ TOA_{M,1} & TOA_{M,2} & \dots & TOA_{M,N} & (x_M, y_M) \end{bmatrix} \quad (18)$$

In the online phase, the device collects the TOA data at the target location and inputs it into the pretrained model to estimate the corresponding coordinates. The estimated position is then returned to the user as the final output, thus completing the localization process. The overall workflow is illustrated in Fig. 7.

3.2 TOA Fingerprint Localization Algorithm Based on CNN-SA-LSTM

- Construction of the Overall Model

In real-world localization scenarios, TOA data is often affected by environmental noise and NLOS errors. When directly applied to traditional trilateration algorithms, such distortions can significantly degrade positioning accuracy. To mitigate these issues, the geometric localization approach is transformed into a fingerprint matching approach by constructing a TOA fingerprint database, thereby reducing the impact of complex environmental interference.

Furthermore, to address the limitations of conventional methods that rely on single-time-point data, we propose a TOA fingerprint localization algorithm based on deep learning. The method integrates spatial and temporal features using a CNN-SA-LSTM network architecture to achieve higher-precision coordinate estimation.

From a model design perspective, CNN are first employed to extract local spatial features from TOA data, enabling the identification of discriminative patterns between different locations. Since CNNs are not inherently capable of modeling temporal sequences, LSTM networks are introduced to capture the sequential dependencies of TOA measurements, thereby improving the model's responsiveness to signal variations in dynamic environments.

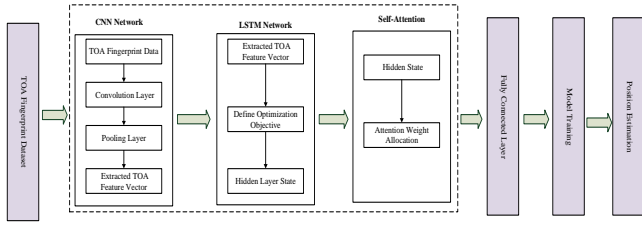


Fig. 8. Overall architecture of the proposed CNN-SA-LSTM-based TOA fingerprint localization algorithm.

To further enhance the model's attention to critical information, a Self-Attention mechanism is incorporated. This allows for dynamic adjustment of feature weights, emphasizing the components that have the greatest impact on localization accuracy. The overall architecture of the proposed algorithm is illustrated in Fig. 8.

- Design and Implementation of the CNN Model

TOA data essentially comprises multiple time values measured by sensors at various reference nodes. Each TOA value depends on the spatial location of the reference point and the distance between the signal source and the sensor. In practice, TOA measurements often fluctuate over time due to environmental dynamics, making TOA data a form of time series. The temporal variation patterns embedded within TOA sequences contain substantial informative value for localization tasks.

Given this, TOA input data can be regarded and processed as temporal sequences. The recorded trajectory information for the input sample can be formally represented as follows:

$$\mathbf{R} = \begin{bmatrix} \text{TOA}_{1,1} & \text{TOA}_{1,2} & \cdots & \text{TOA}_{1,N} \\ \text{TOA}_{2,1} & \text{TOA}_{2,2} & \cdots & \text{TOA}_{2,N} \\ \vdots & \vdots & \ddots & \vdots \\ \text{TOA}_{T,1} & \text{TOA}_{T,2} & \cdots & \text{TOA}_{T,N} \end{bmatrix} \quad (19)$$

where N represents the total number of base stations, and T denotes the trajectory length. Each element in matrix \mathbf{R} corresponds to the TOA value received by a reference node at a specific time. Each row of the matrix represents TOA values received from different sensors at the same time, while each column corresponds to TOA values received by the same sensor across different time points. Therefore, TOA data inherently captures both the spatial relationships among reference nodes and the temporal patterns over time. To effectively perform localization tasks, it is essential that TOA feature extraction methods are capable of capturing both spatial and temporal characteristics.

As shown in Fig. 9, the CNN network is used to extract spatial features. The TOA data is input in matrix form, where each element corresponds to the TOA value of a reference node. In the feature extraction process, two 1D convolutional layers are applied to capture local spatial patterns. Each layer employs 32 convolution kernels of size 3×1 , and zero-padding is used to preserve the dimensionality of the feature maps.

Subsequently, a ReLU activation function is applied to enhance the model's ability to express nonlinearity, improv-

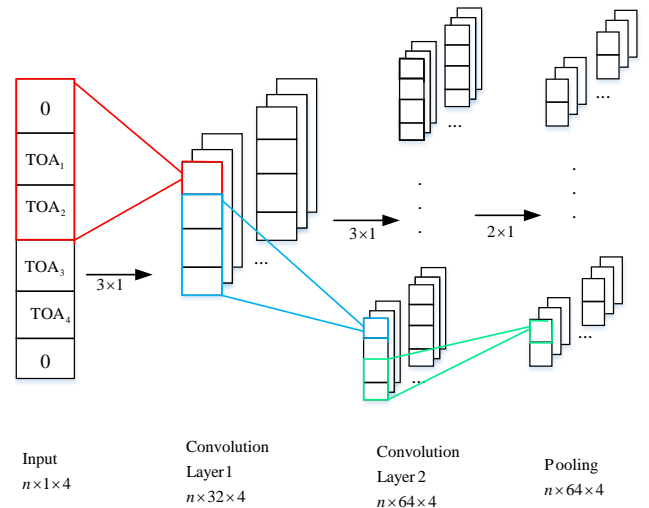


Fig. 9. Structural design of the CNN model.

ing the recognition of complex patterns. To reduce feature dimensionality and prevent overfitting, a max pooling operation with a window size of 2×1 is used in the second convolutional layer. This helps aggregate key features and improves feature extraction efficiency.

- Design and Implementation of the SA-LSTM Model

During the operation of the LSTM model, the TOA feature sequence output from the pooling layer of the CNN network is denoted as \mathbf{x}_t . Each LSTM unit receives both the current time step input \mathbf{x}_t and the hidden state \mathbf{h}_{t-1} , along with the cell state \mathbf{c}_{t-1} from the previous time step. These components are updated through three gating mechanisms that regulate the hidden state \mathbf{h}_t and the cell state \mathbf{c}_t . The detailed steps are as follows:

(1) First, the input data passes through a forget gate, which selects which information from the previous state should be discarded:

$$\mathbf{f}_t = \sigma(\mathbf{W}_f \cdot [\mathbf{x}_t, \mathbf{h}_{t-1}] + \mathbf{b}_f) \quad (20)$$

where σ denotes the sigmoid activation function, and $\mathbf{W}_f, \mathbf{b}_f$ are the weight matrix and bias, respectively. The output \mathbf{f}_t is a vector in the range $[0, 1]$, used to control how much of the previous cell state should be retained at each location.

(2) Next, the input gate combines the current input and candidate values to update the cell state with new information:

a) Compute candidate values for the cell state:

$$\mathbf{c}'_t = \tanh(\mathbf{W}_c \cdot [\mathbf{h}_{t-1}, \mathbf{x}_t] + \mathbf{b}_c) \quad (21)$$

b) Determine the update ratio for new information:

$$\mathbf{i}_t = \sigma(\mathbf{W}_i \cdot [\mathbf{h}_{t-1}, \mathbf{x}_t] + \mathbf{b}_i) \quad (22)$$

c) Update the cell state using both retained and new information:

$$\mathbf{c}_t = \mathbf{f}_t \odot \mathbf{c}_{t-1} + \mathbf{i}_t \odot \mathbf{c}'_t \quad (23)$$

where \odot denotes element-wise multiplication.

(3) Finally, the output gate controls which part of the updated cell state should be output to fulfill the current task:

$$\mathbf{o}_t = \sigma(\mathbf{W}_o \cdot [\mathbf{h}_{t-1}, \mathbf{x}_t] + \mathbf{b}_o). \quad (24)$$

The hidden state is then updated as follows:

$$\mathbf{h}_t = \mathbf{o}_t \odot \tanh(\mathbf{c}_t). \quad (25)$$

Through this LSTM processing, each hidden state \mathbf{h}_t not only serves as the output for the current time step but also participates in the computation of subsequent time steps. This enables dynamic information flow across the entire temporal sequence.

Although LSTM networks offer significant advantages in modeling temporal sequences, relying solely on LSTM for feature extraction still presents certain limitations. To address the issue of inaccurate information focus during long-sequence processing with LSTM, a Self-Attention mechanism is introduced to further optimize the LSTM network.

The Self-Attention mechanism enables the model to directly access information from all time steps, rather than depending exclusively on the hidden states propagated through LSTM layers. This allows the model to identify and emphasize the most critical portions of the entire time sequence by assigning greater weights to key time steps. By computing the contribution weights of different time steps toward the final position estimation, the Self-Attention mechanism effectively highlights feature information that is highly correlated with the target location, thereby enhancing localization accuracy. The architecture of the proposed SA-LSTM localization model is illustrated in Fig. 10.

After completing the design of the full CNN-SA-LSTM network architecture, it is necessary to train the model using an appropriate dataset. The dataset used for training consists of TOA fingerprint data paired with their

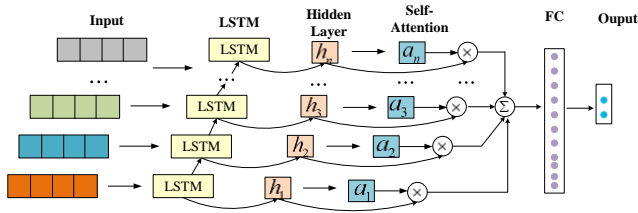


Fig. 10. Architecture of the SA-LSTM localization model.

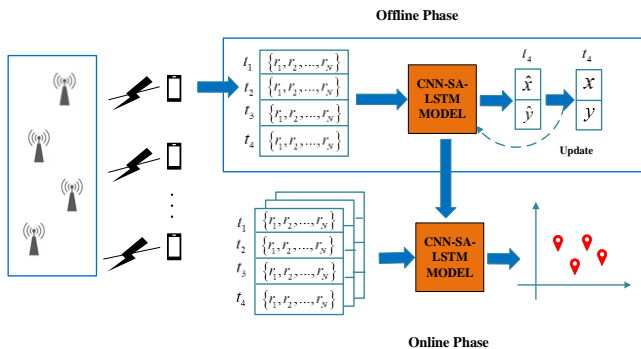


Fig. 11. Principle diagram of localization based on CNN-SA-LSTM.

corresponding spatial coordinates. Through this training process, the model learns the nonlinear mapping relationship between input features and target outputs.

When coordinate estimation is required for a new point, the TOA data collected from the target location is directly fed into the trained CNN-SA-LSTM model, which then outputs the predicted coordinates. The overall localization principle of this approach is illustrated in Fig. 11.

4. Design of a Particle Filter-Based AOA/TOA Fusion Localization Algorithm

In complex and dynamic indoor environments, a single localization technique often fails to simultaneously satisfy the requirements of high accuracy and robustness. AOA-based localization can achieve high precision under favorable LOS conditions, but its performance degrades significantly in large-angle measurement scenarios due to environmental interference. In contrast, TOA fingerprinting offers better adaptability and stronger stability under varying conditions, albeit with slightly lower accuracy.

Therefore, fusing AOA and TOA information can effectively combine their complementary strengths—enhancing localization accuracy while improving system robustness. Moreover, due to the high density of obstacles typically present in indoor environments, signal propagation is inevitably affected by non-Gaussian noise. In such nonlinear and non-Gaussian scenarios, Particle Filter (PF) demonstrates superior performance over methods like the Extended Kalman Filter (EKF) and Unscented Kalman Filter (UKF), especially in handling complex noise distributions and nonlinearities. Accordingly, this study proposes a particle filter-based AOA/TOA fusion localization algorithm, aiming to improve both accuracy and robustness in indoor positioning systems.

4.1 Particle Filtering Algorithm

Particle filtering is a statistical filtering method derived from the principles of the Bayesian filter. It provides an optimal solution for state estimation problems in nonlinear and non-Gaussian systems. The fundamental idea of particle filtering is to approximate the posterior probability distribution of the system state by a set of discrete particles. These particles are then updated iteratively using importance sampling and resampling strategies to progressively estimate the system state.

Unlike traditional methods, particle filtering does not rely on linear system models or Gaussian noise assumptions. Therefore, it is well-suited for complex systems with nonlinear and/or non-Gaussian characteristics. In particular, when both the system model and the observation model are nonlinear, particle filtering demonstrates significant advantages.

In theoretical dynamic system analysis, the state-space model is generally composed of two core components: the

state transition model $p(x_t | x_{t-1})$ and the observation model $p(z_t | x_t)$, where $x_t \in \mathbb{R}^n$ represents the system state at time t , and $z_t \in \mathbb{R}^m$ denotes the corresponding observation.

For nonlinear and non-Gaussian processes, the system's state transition and observation models can be expressed as:

$$x_t = f(x_{t-1}, v_t), \quad (26)$$

$$z_t = h(x_t, n_t) \quad (27)$$

where, $v_t \in \mathbb{R}^n$ and $n_t \in \mathbb{R}^m$ represent the process noise and observation noise, respectively. Both are assumed to be independent and follow zero-mean Gaussian distributions with covariances Q_t and R_t . The functions $f: \mathbb{R}^n \rightarrow \mathbb{R}^n$ and $h: \mathbb{R}^n \rightarrow \mathbb{R}^m$ denote the state transition function and observation function of the system, both of which are generally nonlinear mappings.

The goal of particle filtering is to estimate the system state x_t given the observation set Z_t , and obtain its posterior probability distribution $p(x_t | Z_t)$, where Z_t denotes all observations from time 1 to $\{x_t^{(i)}\}_{i=1}^N$. To approximate this posterior distribution, the particle filter uses a set of particles $\{x_t^{(i)}\}_{i=1}^N$, where N is the total number of particles. Each particle represents a possible state in the state space, and the posterior is approximated as:

$$p(x_t | z_{1:t}) \approx \sum_{i=1}^N w_t^i \sigma(x_t - x_t^i) \quad (28)$$

where $\sigma(\cdot)$ is a Dirac delta kernel; $w_t^{(i)}$ is the weight of the i -th particle, satisfying $\sum_{i=1}^N w_t^{(i)} = 1$; $x_t^{(i)}$ is the i -th particle's predicted state at time t , and $x_0^{(i)}$ is the sample drawn from the initial distribution $p(x_0)$; All particles are usually initialized from the system's prior with uniform weights $w_0^{(i)} = 1/N$.

At each time step, the particle filter uses the state transition model $p(x_t | x_{t-1})$ to propagate particles. This process involves simulating the system's dynamics for each particle based on the previous state $x_{t-1}^{(i)}$. The resulting predicted particle $x_t^{(i)}$ is then evaluated against the new observation z_t , and its weight $w_t^{(i)}$ is updated according to the observation model $p(z_t | x_t^{(i)})$, i.e., the likelihood of the observation given the particle's state. Each particle's weight is updated accordingly:

$$w_{t+1}^{(i)} = w_t^{(i)} \cdot p(z_{t+1} | x_{t+1}^{(i)}) \quad (29)$$

where $w_t^{(i)}$ denotes the weight of the i -th particle $x_t^{(i)}$ at the previous time step, and $p(z_{t+1} | x_{t+1}^{(i)})$ is the likelihood of the current observation given the predicted particle state.

During the operation of the particle filter, the weights of some particles may become extremely small, leading to particle degeneration, where a large proportion of particles no longer contribute to the final state estimate. To address this issue, resampling is introduced to maintain particle di-

versity. Resampling selects particles from the current set according to their weights, and generates a new particle set by replicating higher-weight particles, thereby avoiding degeneration. Common resampling strategies include systematic resampling, roulette wheel resampling, and others. At each time step, the particle filter estimates the system state by computing a weighted average over all particles. That is, the optimal state estimate is given by:

$$\hat{x}_{t+1} = \sum_{i=1}^N w_{t+1}^{(i)} \cdot x_{t+1}^{(i)} \quad (30)$$

where N denotes the total number of particles, $w_{t+1}^{(i)}$ is the weight of the i -th particle, and $x_{t+1}^{(i)}$ represents the state of the i -th particle.

4.2 AOA/TOA Fusion Localization Algorithm Based on Particle Filtering

To enhance the precision and reliability of indoor positioning, this section adopts a PF to fuse the outputs of the AOA and TOA fingerprint localization algorithms. By leveraging the strengths of TOA fingerprinting, the system can compensate for large angular errors in AOA estimation, thereby improving the global stability and effective coverage area of AOA localization. Conversely, the advantages of AOA can also be used to refine TOA-based localization results, further enhancing overall accuracy.

Through this complementary optimization strategy, the fusion algorithm is capable of maintaining high performance under varying environmental conditions. The architecture of the proposed AOA/TOA fusion localization algorithm is illustrated in Fig. 12.

The entire localization process using particle filtering can be divided into five main steps: particle initialization,

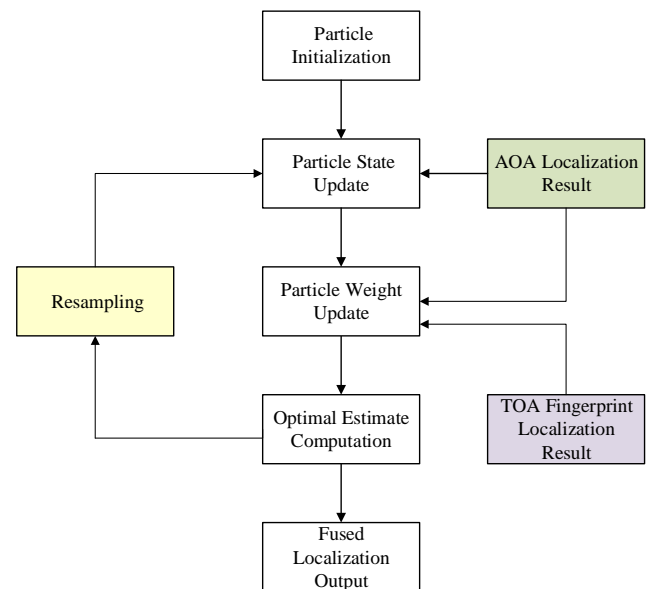


Fig. 12. Framework of the fusion localization algorithm based on Particle Filtering.

state update, weight update, resampling, and optimal state estimation. Each of these steps is described in detail in the following sections.

(1) Particle Initialization

In the proposed algorithm, the particle initialization process relies on the preliminary localization results obtained from AOA-based positioning. The coordinate estimated by the AOA algorithm, denoted as $X_{a,0} = (x_{a,0}, y_{a,0})$, is used as the center of the initial particle distribution. Based on the estimated AOA localization error standard deviation σ , a circular region with radius σ is constructed around this point, representing the uncertainty area.

Within this region, a set of particles is generated according to a Gaussian distribution centered at $X_{a,0}$ with variance σ^2 . Suppose the particle set consists of N_p particles; the initial position of the i -th particle is denoted as $X_i^0 = (x_i^0, y_i^0)$, where $i = 1, 2, \dots, N_p$. To ensure that all particles contribute equally during the first iteration, their initial weights are uniformly set to $1/N_p$. As the iterations proceed, the particle distribution is updated continuously according to the measurement model. Since the initial particle distribution may contain deviations, these errors are gradually corrected through iterative resampling and updates, resulting in reduced impact on the final localization result.

(2) State Update

Since AOA measurements provide only the target's positional coordinates, they do not directly offer information about the target's motion dynamics. Therefore, a suitable motion update model must be constructed to simulate the dynamic behavior of the target during particle propagation. To this end, a pseudo-navigation-based motion model is adopted, enabling prediction of particle states in the absence of direct velocity or direction measurements. This approach enhances the particle filter's capability to capture potential target motion. The specific update formulation for the particle states is detailed as follows:

$$X_t^i = X_{t-1}^i + X_{a,t} - X_{t-1} \quad (31)$$

Let $X_t^i = (x_t^i, y_t^i)$ denote the position of the i -th particle at time t , and $X_{t-1}^i = (x_{t-1}^i, y_{t-1}^i)$ the position at time $t-1$. The coordinate $X_{a,t} = (x_{a,t}, y_{a,t})$ represents the AOA-based localization result at time t , while $X_{t-1} = (x_{t-1}, y_{t-1})$ denotes the final estimated position at time $t-1$ obtained through the particle filter.

By employing this state update strategy, the particle filter combines the historical motion trajectory of each particle with the most recent AOA observation to adjust particle states dynamically. This enables the filter to more effectively track the target's motion behavior in evolving environments.

(3) Particle Weight Update

To mitigate the impact of AOA positioning errors on localization accuracy, a distance-based weight correction mechanism is introduced. As particle weights are continuously adjusted, the resampling and estimation steps of the particle filter progressively converge toward the true target

position. With each iteration, the updated state estimation becomes closer to the target's actual location, thereby enabling more accurate trajectory reconstruction.

a) Initial Weights

During the particle initialization phase, particles are uniformly distributed within a circular region centered at $X_{a,0} = (x_{a,0}, y_{a,0})$, with radius defined by the AOA localization error σ . Assuming that particle locations follow a uniform random distribution within this region, each particle is initially assigned an equal weight of $1/N_p$, where N_p is the total number of particles:

$$w_0^i = \frac{1}{N_p} \quad (32)$$

b) Weight Model Based on TOA Localization

Let the TOA-based estimated position at time t be denoted as (x_t^z, y_t^z) . Particles located closer to the TOA estimation point are assigned higher weights. Since the distribution of particles around the observed value follows a Gaussian distribution, the weight model based on TOA positioning is defined as:

$$\tilde{w}_t^i = \frac{1}{\sqrt{2\pi}\sigma_w} e^{-\frac{d_i^2}{2\sigma_w^2}} \quad (33)$$

where d_i represents the Euclidean distance between the particle (x_t^i, y_t^i) and the TOA observation (x_t^z, y_t^z) . The smaller the distance, the greater the weight. This distance is calculated as:

$$d_i = \sqrt{(x_t^i - x_t^z)^2 + (y_t^i - y_t^z)^2} \quad (34)$$

c) Distance-Based Weighting

The distance-based weight update relies on the spatial distance between the updated particle position and the AOA estimation result. Given the inherent error in AOA based positioning, a threshold-based judgment rule is applied using a distance threshold $\delta = 3\sigma$, where σ denotes the AOA localization error.

If the distance d between the particle's updated position and the AOA estimation is less than δ , the particle is considered reliable and assigned a weight of 1; otherwise, it is assigned a weight of 0. This binary rule ensures that particles significantly deviating from the AOA estimate are discarded. The weighting function is defined as:

$$w_d = \begin{cases} 0, & d > \delta \\ 1, & \text{else} \end{cases} \quad (35)$$

d) Overall Particle Weighting

The overall weight of a particle is determined by the combination of the previously introduced weight components, each reflecting a different factor's influence on the particle. These components are assumed to be independent. If any one of them is zero, the corresponding particle is deemed unreliable and should be discarded, as it cannot contribute meaningful information to the final position estimate.

Accordingly, the overall weight of the i -th particle is calculated as:

$$w_t^i = w_0^i \cdot \tilde{w}_t^i \cdot w_d^i. \quad (36)$$

After multiple iterations, the final weight w_t^i for each particle is obtained. Particles with zero final weight are eliminated from the sample set. The remaining particles are then normalized to ensure that the sum of weights equals 1, using the following normalization equation:

$$\hat{w}_t^i = w_t^i / \sum_{j=1}^n w_t^j. \quad (37)$$

(4) Resampling

After several iterations of particle filtering, the repeated weight updates may lead to weight degeneration—where only a few particles hold significant weights while others approach zero. This effect reduces the effective sample size and can severely impact estimation accuracy. To mitigate this issue, resampling is employed to eliminate particles with low weights and replicate particles with high weights, thereby preserving particle diversity and ensuring stable state estimation. A commonly used approach is random sampling based on the normalized weights of particles.

Specifically, N random numbers are drawn from a uniform distribution $U(0,1)$, sorted in ascending order, and mapped to the cumulative distribution of the particle weights. Let N^i represent the number of samples that fall into the interval $[0, w_t^i]$ for the i -th particle. The larger the weight w_t^i , the greater the probability that more samples will fall into this interval, and hence, the more frequently that particle will be replicated. As a result, particles with high weights are more likely to be retained and duplicated, while those with low weights are likely to be discarded. This process effectively refines the particle set, ensuring that particles with higher credibility are proportionally represented in the final sample population.

(5) Optimal State Estimation

The final position estimate of the filter is obtained by calculating the weighted average of all particles' positions based on their corresponding weights. That is:

$$\hat{X}_t = \sum_{i=1}^N X_t^i \hat{w}_t^i. \quad (38)$$

After each complete round of particle filtering, the AOA estimation result and TOA fingerprinting result are re-introduced as inputs, and the process iterates from step (2) until convergence is achieved.

5. Evaluation

To validate the performance of the proposed algorithm, three sets of experiments were conducted: one for AOA positioning, another for TOA positioning, and a final one for the fusion of AOA and TOA. The system operated at a transmission power of 15 dBm in all experiments, ensuring sufficient signal strength. The antennas used had a gain of

10 dB, which improved signal quality. The system worked at a frequency of 2.4 GHz to optimize signal penetration through walls and provide accurate positioning. These technical parameters were consistent across all three experimental setups.

Furthermore, the proposed concept is designed to work in real time. During the localization process, AOA and TOA data are continuously collected and processed as the user moves through the environment, enabling real-time position estimation. The data processing pipeline consists of two phases. In the offline phase, model parameters are trained using historical data, in the online phase, real-time data from AOA and TOA sensors are fed into the trained models to generate position estimates. The system performs AOA correction, TOA fingerprinting, and AOA/TOA fusion via particle filtering on the fly, ensuring low-latency output suitable for real-time applications. Moreover, the concept can be implemented in real-world systems. Commercially available AOA and TOA sensors can be integrated into base stations and wearable tags, while the computational requirements for real-time processing can be satisfied with embedded processors or edge devices capable of supporting fast inference of the trained models.

5.1 Experimental Results of the AOA Positioning

To validate the performance of the proposed algorithm, experiments were conducted in a meeting room environment. The meeting room has a length of 6 meters and a width of 5 meters. The room contained multiple obstacles such as tables, chairs, and cabinets, as well as a glass wall on one side, in terms of spatial layout, the X-axis direction is represented by blue arrow lines, and the Y-axis direction is represented by green arrow lines, establishing a planar coordinate system, as shown in Fig. 13(a). These elements introduced interference to the AOA signal propagation, resulting in NLOS induced measurement errors. Such conditions align well with the experimental requirements of this study. In this experiment, we used a base station (Model: LD150) and a wristband tag (Model: ULM1-SH) manufactured by Company Dalian Haoru Technology Co., Ltd., as shown in Fig. 14(b). The base station operates with a transmission power of 15 dBm, uses antennas with a gain of 10 dB, and communicates at a frequency of 2.4 GHz. The wristband tag is lightweight, powered by a rechargeable battery with a capacity of 500 mAh, and transmits signals periodically at 100 ms intervals to ensure real-time tracking. In the dynamic localization experiment, a user carried the target tag (as shown in Fig. 14(a)) and moved within the test environment. The approximate movement trajectory is illustrated in Fig. 13(b).

The collected AOA measurements were processed separately using the KF and the GBRT-EN algorithm. The corrected AOA values were then input into the LM and Weighted Least Squares (WLS) algorithms to solve for the user's position coordinates, in order to evaluate the dynamic localization performance. The localization trajectories obtained using the KF+WLS, KF+LM, GBRT-EN+LM, and

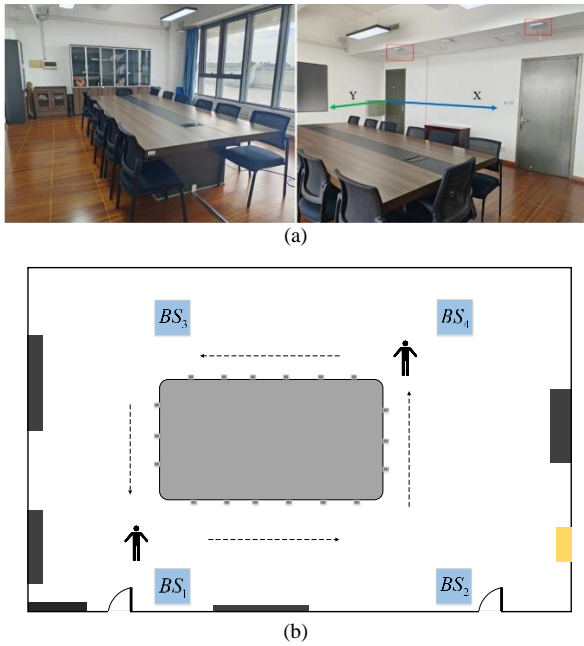


Fig. 13. Actual photograph of the experimental scenario and schematic diagram of the movement trajectory.



Fig. 14. AOA and TOA data experimental equipment.

GBRT-EN+WLS algorithms are depicted in Fig. 15. From the resulting plot, significant fluctuations in the localization data can be observed at route corners. This occurs because at these corner points, one of the four base stations is usually located at a greater distance from the target, resulting in poorer signal quality and substantial angular errors in the AOA measurements, thus adversely impacting position estimation. Additionally, when the user approaches a location with a vertical coordinate of approximately 4.5 m, the carried tag is closest to the glass wall. This inevitably results in signal reflection and refraction, leading to NLOS propagation conditions that degrade positioning accuracy.

As illustrated in Fig. 15(a), preprocessing AOA measurements using the GBRT-EN algorithm significantly improves positioning accuracy compared to processing AOA

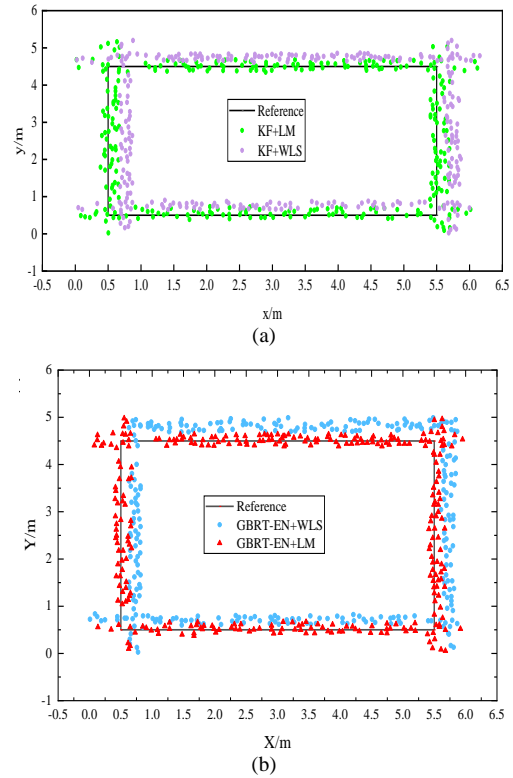


Fig. 15. Comparison of dynamic trajectories under different AOA localization algorithms.

measurements with only the KF algorithm. Furthermore, it is also evident that the LM algorithm yields higher localization accuracy compared to the conventional WLS method, as shown in Fig. 15(b).

Error analysis along the X-axis under different algorithms was conducted. Figure 16(a) presents the error histogram, demonstrating that the overall errors calculated using the GBRT-EN+LM algorithm predominantly fall within the range of 0.10 m to 0.40 m, with a maximum error around 0.60 m. Regarding the Cumulative Distribution Function (CDF) along the X-axis, Figure 16(b) shows the CDF plots for the four localization algorithms. As indicated, approximately 80% of the errors obtained using the GBRT-EN+LM algorithm along the X-axis are within 0.35 m.

Along the Y-axis direction, the overall errors calculated using the GBRT-EN+LM algorithm predominantly lie within the range of 0.10 m to 0.30 m, with the maximum error around 0.60 m. Regarding the CDF along the Y-axis, for errors within 0.45 meters, the cumulative probability of the GBRT-EN+LM algorithm reaches 96.49%.

To further evaluate the performance of different algorithms, the localization errors of four algorithms are presented. As shown in Tab. 1, the average error of the GBRT-EN+LM algorithm is 0.47 meters, which represents a reduction in localization error by 17.54%, 27.69%, and 41.25% compared to the other three algorithms, respectively. These data validate the effectiveness of the proposed algorithm and demonstrate its improvement in positioning accuracy.

In summary, the proposed GBRT-EN combined with the LM algorithm demonstrates superior localization perfor-

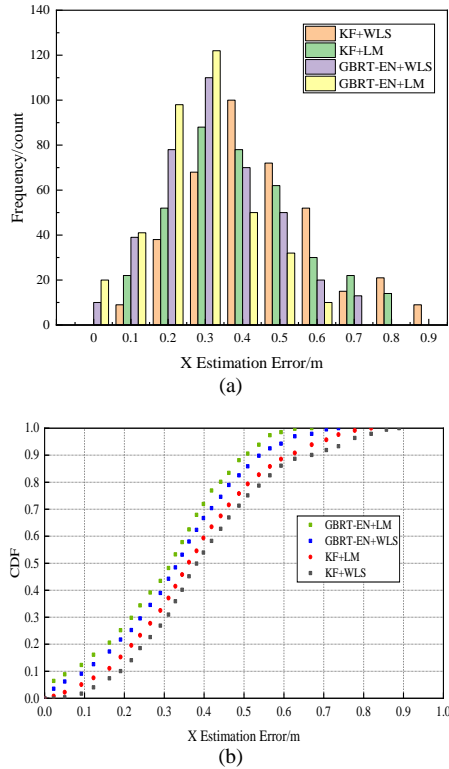


Fig. 16. Distribution histogram and CDF of error along the X-axis.

Algorithms	GBRT+LM	GBRT+WLS	KF+LM	KF+WLS
Maximum Error/m	0.60	0.65	0.74	0.89
Minimum Error/m	0.26	0.48	0.56	0.71
Average Error / m	0.47	0.57	0.65	0.80

Tab. 1. Localization errors for different AOA localization algorithms.

mance in this experiment, effectively enhancing positioning robustness and significantly improving indoor positioning accuracy.

5.2 Experimental Results of the TOA Positioning

To validate the performance of the improved TOA localization algorithm, a walking trajectory test was conducted using the aforementioned experimental setup. The experimenter wore a wristband-type tag (as shown in Fig. 17(b), sampling frequency of 100 Hz) and maintained real-time communication with the base stations. The backend server processed the uploaded TOA data, calculating the distance information of the localization points, and fed this data into the trained CNN-SA-LSTM network model to estimate the target positions. Additionally, the WLS and WKNN algorithms were also applied to process the TOA data, and comparative experiments were conducted. The localization outcomes are illustrated in Fig. 17.

In Fig. 18, the blue solid line represents the pedestrian’s ground truth trajectory, while the purple dots indicate the positions estimated using the WKNN algorithm. Due to

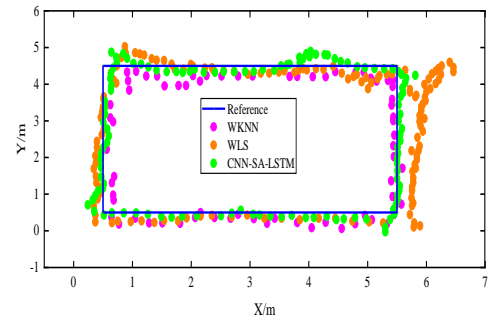


Fig. 17. Dynamic localization trajectories under different TOA-based algorithms.

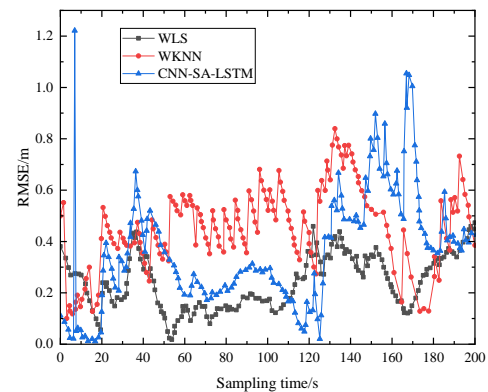


Fig. 18. Comparison of RMSE over time for different TOA-based localization algorithms.

WKNN’s reliance on matching-based positioning, its accuracy is affected by the density of reference points, resulting in overlapping points and relatively sparse position estimations. The orange dots represent localization results calculated by the traditional mathematical method WLS. Notably, a significant drift can be observed near the horizontal coordinate of 6 meters. This deviation is attributed to a glass cabinet at that location, which caused signal reflection and refraction, leading to TOA measurement errors and decreased positioning accuracy. The green dots denote the localization results obtained using the proposed CNN-SA-LSTM algorithm. As evident from the comparison, the CNN-SA-LSTM estimates are closer to the actual trajectory and demonstrate superior performance compared to both WKNN and WLS methods.

Figure 19 illustrates the comparison of distance errors between the estimated positions and the ground truth for the three algorithms. The horizontal axis represents the sampling time, while the vertical axis indicates the RMSE, which serves as a metric to evaluate the accuracy of the localization algorithms.

From the overall distribution of the curves, the WLS algorithm exhibits noticeable fluctuations in positioning error over time. Several significant peaks appear during different time intervals, although in certain segments, WLS still outperforms the CNN-SA-LSTM algorithm. This suggests that the performance of the traditional WLS method is more susceptible to environmental complexity and provides relatively limited robustness in maintaining localization accuracy. In contrast, the RMSE of the WKNN algorithm is gen-

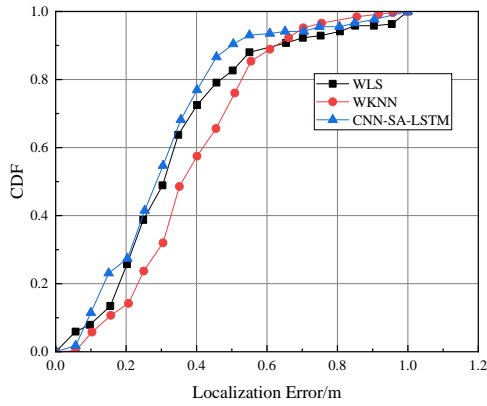


Fig. 19. CDF comparison of localization errors for WLS, WKNN, and CNN-SA-LSTM algorithms.

Algorithm	WLS	WKNN	CNN-SA-LSTM
RMSE/m	0.46	0.52	0.39

Tab. 2. RMSE comparison of different TOA localization algorithms.

erally higher than that of CNN-SA-LSTM throughout the entire time sequence. The elevated RMSE values of WKNN are primarily due to insufficient reference points in areas with complex signal conditions, resulting in increased positioning errors.

Among the three, the CNN-SA-LSTM algorithm demonstrates the smallest RMSE variation and maintains consistently low localization errors across the time series, indicating stronger anti-interference capability and overall robustness.

Figure 19 presents the CDF curves of the three localization algorithms with respect to positioning error. The horizontal axis denotes the localization error, while the vertical axis represents the CDF value, reflecting the distribution of positioning accuracy across different error thresholds. As observed from Fig. 19, for the WLS algorithm, 80% of the positioning errors fall within 0.46 meters. For the WKNN algorithm, 80% of the errors are within 0.54 meters. In comparison, the CNN-SA-LSTM algorithm achieves 80% of localization errors within 0.43 meters.

To visually present the positioning performance of the three localization algorithms, a quantitative analysis is conducted by calculating the RMSE between the estimated trajectory and the true trajectory. Table 2 provides a detailed comparison of the RMSE results for the three localization algorithms along a rectangular motion trajectory.

As shown in Tab. 2, the RMSE between the true and estimated points for the CNN-SA-LSTM algorithm decreased from 0.46 m to 0.39 m, a reduction of 25.00%, compared to the WKNN algorithm. When compared to the WLS algorithm, the RMSE decreased by 15.22%. These results demonstrate that the proposed CNN-SA-LSTM algorithm performs slightly better than the other two traditional localization algorithms.

Based on the CDF analysis and Tab. 2, the CNN-SA-LSTM algorithm demonstrates slightly better overall performance in terms of positioning accuracy compared to the other two methods.

5.3 Experimental Results of the Fusion Positioning

To validate the effectiveness of the proposed fusion algorithm, the experiment involved a pedestrian wearing a TOA tag and holding an AOA tag, walking along a predefined trajectory. The AOA data and TOA fingerprint data collected during the experiment were simultaneously uploaded to the host computer, and then processed using the improved methods presented in Sec. 2 and 3. Finally, the particle filtering algorithm was used to fuse the AOA and TOA localization results, improving positioning accuracy. The final localization results obtained from the three methods are illustrated in Fig. 20.

To quantitatively evaluate the localization performance of the proposed fusion algorithm, the CDF of the dynamic positioning error for the pedestrian was calculated. The resulting CDF curve is shown in Fig. 21.

As shown in the CDF curve, for the TOA fingerprint localization algorithm enhanced by the CNN-SA-LSTM network, 80% of the positioning errors fall within 0.44 meters. For the AOA localization algorithm improved using the GBRT-EN+LM approach, 80% of the errors are within 0.49 meters. In contrast, the particle filter-based fusion method achieves 80% of positioning errors within 0.36 meters. These results demonstrate that the fusion approach offers improved localization accuracy compared to the two standalone methods.

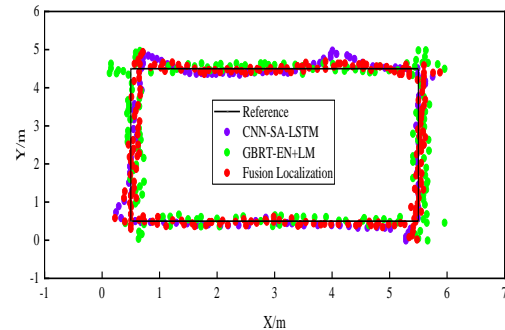


Fig. 20. Comparison of localization results using AOA-only, TOA-only, and AOA/TOA fusion via particle filtering.

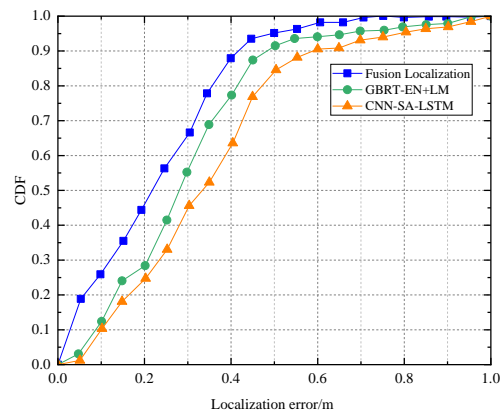


Fig. 21. CDF of dynamic localization error for the fusion algorithm.

Algorithm	Maximum Error/m	Average Error /m	RMSE/m
GBRT-EN+LM	0.95	0.47	0.48
CNN-SA-LSTM	0.83	0.35	0.39
Fusion Algorithm	0.76	0.27	0.31

Tab. 3. Localization error statistics for different localization algorithms.

To further demonstrate the differences in the results of the three localization algorithms, the RMSE between the estimated and true trajectories was quantitatively analyzed. Table 3 provides a detailed comparison of the three algorithms' errors in a short-range motion scenario. As shown in Tab. 3, the fusion localization algorithm achieved a reduction in RMSE by 35.42% and 20.51%, respectively, compared to the two individual localization algorithms. This improvement enhances the positioning accuracy of the indoor localization system.

6. Conclusions

Focusing on the challenge of high-precision localization in complex indoor environments, this study proposes a multi-stage enhancement method that integrates both AOA and TOA information, achieving favorable outcomes in both algorithm design and experimental validation.

Firstly, to address the vulnerability of AOA measurements to interference under NLOS conditions, a hybrid correction mechanism combining GBRT and EN was introduced. This approach effectively suppresses abrupt angular deviations and enhances the robustness of AOA data. However, it should be noted that this hybrid correction mechanism introduces higher computational complexity, which may limit its scalability in large-scale applications. Subsequently, the LM algorithm was employed to efficiently solve for position using the corrected angle measurements, resulting in a significant RMSE reduction of 41.25%.

Secondly, to mitigate the sensitivity of TOA fingerprinting to environmental noise, a deep learning model integrating CNN, LSTM networks, and a Self-Attention mechanism was constructed. This model captures the spatio-temporal dependencies in TOA data, endowing it with strong adaptability and generalization capabilities. Experimental results show that the proposed model reduces RMSE by 15.22% and 25.00% compared to the WLS and WKNN algorithms, respectively.

Finally, a fusion strategy based on the PF algorithm was developed to integrate AOA and TOA positioning results. By fully leveraging the complementary advantages of both localization modalities, the fusion method achieves superior error correction and state estimation across various environments. However, the PF-based fusion strategy may encounter challenges in real-time applications due to increased processing time and computational complexity. Ultimately, the system achieves further RMSE reductions of 35.42% and 20.51%, compared to the single-modality AOA and TOA approaches, respectively.

In future work, we will explore the generalization capability of the model under multi-scenario, multi-user, and

multi-device collaborative settings. Additionally, we will investigate the incorporation of lightweight neural network architectures and GNN to enhance deployment efficiency and real-time performance, laying the foundation for building more adaptive and intelligent indoor localization systems.

Furthermore, due to the limitations of the experimental setup in this study, we were unable to evaluate the effect of different base station configurations on system performance. As a next step, we plan to examine how varying base station locations and configurations may influence localization accuracy, robustness, and overall effectiveness. This will provide deeper insights into the practical applicability and scalability of the algorithm in real-world environments. We also plan to address the aforementioned challenges, such as computational complexity and real-time processing, to further improve the method's applicability in large-scale, dynamic settings. More detailed information about the mathematical model and the source code used in this study is available from the corresponding author upon reasonable request.

Acknowledgments

This work was supported in part by the "Pioneer" and "Leading Goose" R&D Program of Zhejiang Province (Grant No. 2023C01030) and the Research Project of Zhejiang Provincial Department of Education (Grant No. Y202558237), in part by the National Natural Science Foundation of China (Grant No. 62071212 and 62371218), and in part by the open project of Guangdong Provincial Key Laboratory of Advanced Wireless Communications (Southern Univ. of Science and Technology Shenzhen 518055, China).

References

- [1] TIMOFEEV, A. L., SULTANOV, A. K., MESHKOV, I. K., et al. Increasing the positioning accuracy of the GLONASS system. *Siberian Aerospace Journal*, 2024, vol. 25, no. 4, p. 482–492. DOI: 10.31772/2712-8970-2024-25-4-482-492
- [2] LI, G. D., JIN, J., WANG, F., et al. Efficient path planning algorithm using topology for indoor environment (in Chinese). *Computer Engineering*, 2022, vol. 48, p. 95–106. DOI: 10.19678/j.issn.1000-3428.0061761
- [3] ASAAD, S. M., MAGHDID, H. S. A comprehensive review of indoor/outdoor localization solutions in IoT era: Research challenges and future perspectives. *Computer Networks*, 2022, vol. 212, p. 1–28. DOI: 10.1016/j.comnet.2022.109041
- [4] FARAHSAARI, P. S., FARAHZADI, A., REZAZADEH, J., et al. A survey on indoor positioning systems for IoT-based applications. *IEEE Internet of Things Journal*, 2022, vol. 9, no. 10, p. 7680–7699. DOI: 10.1109/JIOT.2022.3149048
- [5] ROY, P., CHOWDHURY, C. A survey on ubiquitous WiFi-based indoor localization system for smartphone users from implementation perspectives. *CCF Transactions on Pervasive Computing and Interaction*, 2022, vol. 4, no. 3, p. 298–318. DOI: 10.1007/s42486-022-00089-3
- [6] PANJA, A. K., KARIM, S. F., NEOGY, S., et al. Improving the sustainability of WiFi-enabled indoor localization systems through

- meta-heuristic based instance selection approach. *Expert Systems with Applications*, 2024, vol. 257, p. 1–14. DOI: 10.1016/j.eswa.2024.125063
- [7] RIZZI, M., FERRARI, P., FLAMMINI, A., et al. Evaluation of the IoT LoRaWAN solution for distributed measurement applications. *IEEE Transactions on Instrumentation and Measurement*, 2017, vol. 66, no. 12, p. 3340–3349. DOI: 10.1109/TIM.2017.2746378
- [8] MORADBEIKIE, A., ZARE, M., KESHAVARZ, A., et al. RSSI-based LoRaWAN dataset collected in a dynamic and harsh industrial environment with high humidity. *Data in Brief*, 2024, vol. 53, p. 1–8. DOI: 10.1016/j.dib.2024.110120
- [9] DALVEREN, Y., KARA, A. Multipath exploitation in emitter localization for irregular terrains. *Radioengineering*, 2019, vol. 28, no. 2, p. 473–482. DOI: 10.13164/re.2019.0473
- [10] WU, P. Comparison between the ultra-wide band based indoor positioning technology and other technologies. *Journal of Physics: Conference Series*, 2022, vol. 2187, p. 1–8. DOI: 10.1088/1742-6596/2187/1/012010
- [11] LIU, Z., CHEN, L., ZHOU, X., et al. Machine learning for time-of-arrival estimation with 5G signals in indoor positioning. *IEEE Internet of Things Journal*, 2023, vol. 10, no. 11, p. 9782–9795. DOI: 10.1109/IJOT.2023.3234123
- [12] WAN, Q., WU, T., ZHANG, K., et al. A high precision indoor positioning system of BLE AOA based on ISSS algorithm. *Measurement*, 2024, vol. 224, p. 1–16. DOI: 10.1016/j.measurement.2023.113801
- [13] FURFARI, F., GIROLAMI, M., MAVILIA, F., et al. Indoor localization algorithms based on angle of arrival with a benchmark comparison. *Ad Hoc Networks*, 2025, vol. 166, p. 1–16. DOI: 10.1016/j.adhoc.2024.103691
- [14] ZHANG, Z., WANG, D., YANG, B., et al. Weighted multidimensional scaling localization method with bias reduction based on TOA. *IEEE Sensors Journal*, 2023, vol. 23, no. 17, p. 19803–19814. DOI: 10.1109/JSEN.2023.3296986
- [15] ZAIDI, M., BOUAZZI, I., USMAN, M., et al. Cooperative scheme ToA-RSSI and variable anchor positions for sensors localization in 2D environments. *Complexity*, 2022, no. 1, p. 1–11 DOI: 10.1155/2022/5069254
- [16] WANG, W., WANG, G., HO, K. C., et al. Robust TDOA localization based on maximum correntropy criterion with variable center. *Signal Processing*, 2023, vol. 205, p. 1–9. DOI: 10.1016/j.sigpro.2022.108860
- [17] ÇELİK, E. IEGQO-AOA: Information-exchanged Gaussian arithmetic optimization algorithm with quasi-opposition learning. *Knowledge-Based Systems*, 2023, vol. 260, p. 1–18. DOI: 10.1016/j.knsys.2022.110169
- [18] SHANG, S., WANG, L. Overview of WiFi fingerprinting-based indoor positioning. *IET Communications*, 2022, vol. 16, no. 7, p. 725–733. DOI: 10.1049/cmu2.12386
- [19] CAO, H., WANG, Y., BI, J., et al. LOS compensation and trusted NLOS recognition assisted WiFi RTT indoor positioning algorithm. *Expert Systems with Applications*, 2024, vol. 243, p. 1–12. DOI: 10.1016/j.eswa.2023.122867
- [20] CHEN, X., FENG, Z., WEI, Z., et al. Multiple signal classification based joint communication and sensing system. *IEEE Transactions on Wireless Communications*, 2023, vol. 22, no. 10, p. 6504–6517. DOI: 10.1109/TWC.2023.3244195
- [21] GAO, F., GERSHMAN, A. B. A generalized ESPRIT approach to direction-of-arrival estimation. *IEEE Signal Processing Letters*, 2005, vol. 12, no. 3, p. 254–257. DOI: 10.1109/LSP.2004.842276
- [22] DENG, W., LI, J., TANG, Y., et al. Low-complexity joint angle of arrival and time of arrival estimation of multipath signal in UWB system. *Sensors*, 2023, vol. 23, no. 14, p. 1–15. DOI: 10.3390/s23146363
- [23] WANG, K., LI, B. Research on AOA/Snell indoor fusion positioning algorithm with NLOS error compensation. In *2024 IEEE 7th Advanced Information Technology, Electronic and Automation Control Conference (IAEAC)*. Chongqing (China), 2024, p. 332–336. DOI: 10.1109/IAEAC59436.2024.10504027
- [24] KOIVISTO, M., TALVITIE, J., COSTA, M., et al. Joint cm wave-based multiuser positioning and network synchronization in dense 5G networks. In *IEEE Wireless Communications and Networking Conference (WCNC)*. Barcelona (Spain), 2018, p. 1–6. DOI: 10.1109/WCNC.2018.8377435
- [25] XIAO, K., HAO, F., ZHANG, W., et al. Research and implementation of indoor positioning algorithm based on Bluetooth 5.1 AOA and AOD. *Sensors*, 2024, vol. 24, no. 14, p. 1–17. DOI: 10.3390/s24144579
- [26] LIU, J., WANG, T., LI, Y., et al. A transformer-based signal denoising network for AoA estimation in NLoS environments. *IEEE Communications Letters*, 2022, vol. 26, no. 10, p. 2336–2339. DOI: 10.1109/LCOMM.2022.3187661
- [27] FENG, Y. L., LI, M. Z., LI, J., et al. Edge cloud resource scheduling with deep reinforcement learning. *Radioengineering*, 2025, vol. 34, no. 1, p. 92–108. DOI: 10.13164/re.2025.0092
- [28] LIU, G., KANG, Y., QUAN, H., et al. The detection performance of the dual-sequence-frequency-hopping signal via stochastic resonance processing under color noise. *Radioengineering*, 2019, vol. 27, no. 3, p. 618–626. DOI: 10.13164/re.2019.0618
- [29] ZHOU, Z., LI, S., LIU, Y. Study on AOA location algorithm based on machine learning optimization. In *International Conference on Microwave and Millimeter Wave Technology (ICMMT)*. Beijing (China), 2024, vol. 1, p. 1–3. DOI: 10.1109/ICMMT61774.2024.10671996
- [30] SCHANTZ, H. *The Art and Science of Ultrawideband Antennas*, 2nd ed. Beijing (China): Posts & Telecom Press, 2012, ISBN: 9787115262110
- [31] ZHAO, R., ZHANG, H., LIN, Q., et al. *UWB Positioning Technology and Its Applications in Smart Manufacturing*. (in Chinese) Beijing (China): China Machine Press, 2020. ISBN: 9787111667445

About the Authors ...

Xiaoli YAO (corresponding author) was born in Anhui Province, China in 1991. She received her Ph.D. in Electronic Science and Technology from Hangzhou Dianzi University in 2020. She is currently a lecturer at Zhejiang Polytechnic University of Mechanical and Electrical Engineering, and her research focuses on deep learning and fusion positioning.

Zhijiang XU (corresponding author) was born in 1973. He received his Ph.D. in Information and Communication Engineering in 2005 from Zhejiang University, China. He was appointed Associate Professor in the College of Information Engineering at Zhejiang University of Technology, China, from 2007 to 2019. Since 2019, he has joined the Zhejiang Polytechnic University of Mechanical and Electrical Engineering in the School of Automation and was promoted to full Professor in 2020. His research interests include digital communications over fading channels, channel modeling, coding, digital synchronization, etc.

Fangfang QIANG was born in Zhejiang Province, China in September 1992. She received her Ph.D. degree in Electronic Science and Technology from Hangzhou Dianzi University in 2020. She is now a lecturer at Zhejiang University of Science and Technology, specializing in intelligent signal processing and computer vision.